NASA-TM-102,730

NASA Technical Memorandum 102730

NASA-TM-102730 19910002360

DEVELOPMENT OF UNSTRUCTURED GRID METHODS FOR STEADY AND UNSTEADY AERODYNAMIC ANALYSIS

JOHN T. BATINA

NOVEMBER 1990

LIBRARY COPY

NOV 0 1 1990

LANGLEY RESEARCH CENTER
LIBRARY NASA
HAMPTON, VIRGINIA

FOR REFERENCE

[illegible]

NOT TO BE TAKEN FROM THIS ROOM

NASA
National Aeronautics and
Space Administration

Langley Research Center
Hampton, Virginia 23665

DEVELOPMENT OF UNSTRUCTURED GRID METHODS FOR STEADY AND UNSTEADY AERODYNAMIC ANALYSIS

John T. Batina*
NASA Langley Research Center
Hampton, Virginia 23665-5225 USA

Abstract

The current status of the development of unstructured grid methods in the Unsteady Aerodynamics Branch at NASA Langley Research Center is described. These methods are being developed for steady and unsteady aerodynamic applications. The paper first highlights the flow solvers that have been developed for the solution of the unsteady Euler and Navier-Stokes equations and then gives selected results which demonstrate various features of the capability. The results demonstrate two- and three-dimensional applications for both steady and unsteady flows. Comparisons are also made with solutions obtained using a structured grid code and with experimental data to determine the accuracy of the unstructured grid methodology. These comparisons show good agreement which thus verifies the accuracy.

Introduction

Considerable progress has been made over the past two decades on developing computational fluid dynamics (CFD) methods for aerodynamic analysis.[1,2] Recent work in CFD has focused primarily on developing algorithms for the solution of the Euler and Navier-Stokes equations. For unsteady aerodynamic and aeroelastic analysis, these methods generally require that the mesh move to conform to the instantaneous position of the moving or deforming body under consideration. Many of the methods that are currently being developed assume that the mesh moves rigidly or that the mesh shears as the body deforms. These assumptions consequently limit the applicability of the procedures to rigid-body motions or small-amplitude deformations. Furthermore, these methods of solution typically assume that the computational grid has an underlying geometrical structure. As an alternative, algorithms have been developed recently which make use of unstructured grids.[3-16] In two dimensions these grids are typically made up of triangles and in three dimensions they consist of an assemblage of tetrahedra. The unstructured grid methods have several distinct advantages over structured grid methods which make them attractive for unsteady aerodynamic and aeroelastic analyses. For example, the primary advantage of the unstructured grid methodology is the ability to easily model very complicated three-dimensional configurations with virtually unlimited geometrical complexity. A second advantage is that the methodology allows for a general way to move the mesh to treat realistic motions and structural deformations of complete aircraft configurations. The deforming grid capability does not involve any assumptions which limit applications to small deformations, such as simple grid shearings which are done in some structured grid codes. A third advantage is that it enables in a natural way for adaptive mesh refinement to more accurately predict the physics of the flow. Highly accurate solutions may thus be obtained by using far fewer grid points than if a globally fine mesh was used.

The purpose of the paper is to describe the current status of the development of unstructured grid methods within the Unsteady Aerodynamics Branch at NASA Langley Research Center.[10-16] The paper first highlights the flow solvers that have been developed for solution of the time-dependent Euler and Navier-Stokes equations and then gives selected results which demonstrate various features of the capability. The flow solvers that are described are either of the central-difference-type with explicit artificial dissipation or of the upwind-type which are naturally dissipative. Both implicit and explicit temporal discretizations are discussed for the time-integration of the governing fluid flow equations. Details on the adaptive mesh refinement procedures are also given. The selected results that are presented demonstrate two- and three-dimensional applications for both steady and unsteady flows. Comparisons are also made with solutions obtained using a structured grid code and with experimental data to determine the accuracy of the unstructured grid methodology.

Central-Difference-Type Flow Solver

The unsteady Euler equations in integral form are solved using a finite-volume algorithm that was developed for use on unstructured grids of triangles in 2D or tetrahedra in 3D.[10-13] The algorithm reduces conceptually to central differencing on a rectangular mesh and thus is referred to as a central-difference-type flow solver. With this solver, artificial dissipation is added explicitly to prevent oscillations near shock waves and to damp high-frequency uncoupled error modes. Specifically, an adaptive blend of harmonic and biharmonic operators is used, corresponding to second and fourth difference dissipation, respectively. The biharmonic operator provides a background dissipation to damp high frequency errors and the harmonic operator prevents oscillations near shock waves.

The Euler equations are integrated in time using a standard, explicit, four-stage, Runge-Kutta time-stepping scheme. In this scheme the convective operator is evaluated at each stage and, for computational efficiency, the dissipative operator is evaluated only at the first stage. The scheme is second-order-accurate in time and includes the necessary terms to account for changes in cell volumes due to a moving or deforming mesh. Furthermore, this explicit scheme has a step size that is limited by the Courant-Friedricks-Lewy (CFL) condition corresponding to a CFL number of $2\sqrt{2}$. To accelerate convergence to steady-state, the CFL number may be increased by averaging implicitly the residual with values at neighboring grid points. These implicit equations are solved approximately using several Jacobi iterations. Convergence to steady-state is further accelerated using enthalpy damping and local time stepping. The local time stepping uses a maximum allowable step size at each grid point as determined by a local stability analysis. For unsteady applications, however, a global time step is usually used because of the time-accuracy requirement. The maximum allowable global time step may be increased to a value that is larger than that dictated by the CFL condition, by using a time accurate version of the residual smoothing.

If interest is restricted to supersonic flow past conical bodies, then the conical flow assumption can be made. This reduces the problem from three dimensions to two dimensions, which significantly decreases the computational resources that are required to investigate such flows. The conical flow assumption is exact for inviscid supersonic flow and is used to efficiently investigate vortex-dominated flows. For viscous

---

*Senior Research Scientist, Unsteady Aerodynamics Branch, Structural Dynamics Division

N91-11673#

flow, however, a length dependence remains in the Reynolds number (Re), although the flow may be considered to be locally conical. The Reynolds number therefore determines the location of the plane at which the solution is determined. Conical Euler and Navier-Stokes solvers have been developed based on a central-difference-type spatial discretization,[13] similar to the two- and three-dimensional Euler solvers described above. The viscous fluxes in the conical Navier-Stokes solver are evaluated by first computing derivatives of the velocity components required by the shear stresses and heat flux terms using Green's theorem. Once evaluated, these fluxes are averaged across edges in the same manner as the inviscid fluxes. Also, the viscous fluxes are computed only at the first stage of the Runge-Kutta time-marching scheme for computational efficiency. This effectively reduces the computational work to evaluate the viscous fluxes by a factor of four.

Upwind-Type Flow Solver

The unsteady Euler equations may be solved alternatively by using upwind differencing and either flux-vector or flux-difference splitting similar to upwind schemes developed for use on structured meshes.[10,14-16] The present unstructured grid algorithm is thus referred to as an upwind-type flow solver. The spatial discretization of this solver involves a so-called flux-split approach based on either the flux-vector splitting of van Leer[17] or the flux-difference splitting of Roe.[18] These flux-split discretizations account for the local wave-propagation characteristics of the flow and they capture shock waves sharply with at most one grid point within the shock structure. A further advantage is that these discretizations are naturally dissipative and consequently do not require additional artificial dissipation terms or the adjustment of free parameters to control the dissipation. However, in calculations involving higher-order upwind schemes such as these, oscillations in the solution near shock waves are expected to occur. To eliminate these oscillations flux limiting is usually required. In the present study, a continuously differentiable flux limiter was employed.[14-16]

The Euler equations are integrated in time using either an explicit Runge-Kutta method (described in the previous section) or an implicit time-integration scheme involving a Gauss-Seidel relaxation procedure.[14] The procedure is implemented by re-ordering the elements that make up the unstructured mesh from upstream to downstream. The solution is obtained by sweeping two times through the mesh as dictated by stability considerations. The first sweep is performed in the direction from upsteam to downstream and the second sweep is from downstream to upstream. For purely supersonic flows the second sweep is unnecessary. This relaxation scheme is stable for large time steps and thus allows the selection of the step size based on the temporal accuracy of the problem being considered, rather than on the numerical stability of the algorithm. Consequently, very large time steps may be used for rapid convergence to steady state, and an appropriate step size may be selected for unsteady cases, independent of numerical stability issues.

Spatial Adaption Procedure

Spatial adaption is employed with the unstructured grid flow solvers to enrich the mesh locally in regions of high spatial flow gradients to more accurately and efficiently resolve the physics of the flow.[13] Equally attractive are coarsening techniques that remove elements from regions where relatively small changes in the flow variables occur. Both enrichment and coarsening procedures are currently being developed. However, only the enrichment procedure is described as follows.

A refinement indicator is used to determine if an element in the mesh is to be refined or subdivided into smaller elements. Typically, the absolute change in density along an edge is used as an indicator for flows with shock waves and total pressure loss is used for flows with vortices. The refinement indicator is compared with a preset tolerance to determine whether a given element should be refined. If the tolerance is exceeded, a new node is created at the midpoint of the edge and the element is divided. Each time the mesh is refined, an element may be divided in one of several different ways. The coordinates of the new node are determined by averaging the coordinates of the endpoints that make up the bisected edge. Special care must be taken, however, when an edge that is to be divided lies on a boundary of the grid, since the midpoint of the edge does not generally lie on the boundary. In this case, the location of the new node is determined generally by using a spline of the boundary coordinates.

Deforming Mesh Algorithm

For problems where the aircraft moves or deforms, the mesh must move so that it continuously conforms to the instantaneous shape or position of the vehicle. This is accomplished by using a spring network to model the original mesh such that each edge of the triangle or tetrahedron is represented by a spring.[12] The spring stiffness for a given edge is taken to be inversely proportional to the length of the edge. Grid points on the outer boundary of the mesh are held fixed and the instantaneous locations of the points on the inner boundary (aircraft) are given by the prescribed surface motion. At each time step, the static equilibrium equations in the x, y, and z directions, which result from a summation of forces, are solved iteratively at each interior node of the grid for the displacements. This is accomplished by using a predictor-corrector procedure, which first predicts the displacements of the nodes by extrapolation from grids at previous time levels and then corrects these displacements using several Jacobi iterations of the static equilibrium equations. The predictor-corrector procedure has been found to be more efficient than simply performing Jacobi iterations because far fewer iterations are required to achieve acceptable convergence. In practice, it has been found that only one or two iterations are sufficient to accurately move the mesh.

Results and Discussion

Selected results from the unstructured grid methods of Refs. 10-16 are presented for two- and three-dimensional

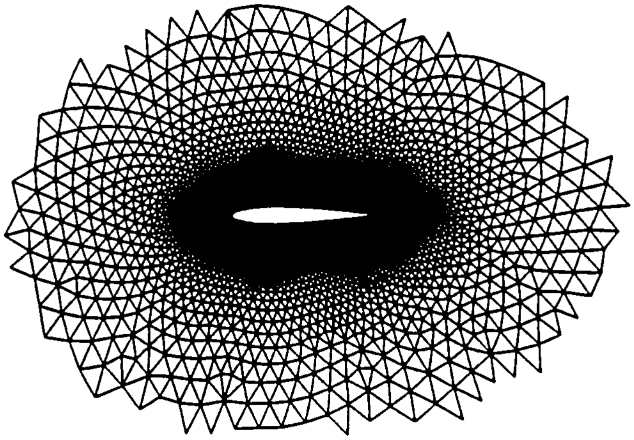

Fig. 1 Partial view of unstructured grid of triangles about the NACA 0012 airfoil.

geometries for both steady and unsteady flows. Comparisons are made with solutions obtained using a structured grid code and with experimental data to determine the accuracy of the methodology.

Two-Dimensional Euler Results

To assess the two dimensional central-difference and upwind-type Euler solvers, calculations were performed for the NACA 0012 airfoil. These results were obtained by using the unstructured grid shown in Fig. 1 which was generated using the advancing front method.[6,7] The grid has 3300 nodes, 6466 triangles, and extends 20 chordlengths from the airfoil with a circular outer boundary. Also there are 110 points that lie on the airfoil surface. This is the same mesh that was used to obtain the results that were presented in Refs. 10, 11, and 14.

Generalized aerodynamic forces were obtained using the central-difference-type Euler solver for the NACA 0012 airfoil oscillating in either plunge or pitch-about-the-quarter-chord to determine the accuracy of the unstructured grid method for unsteady aerodynamic applications. Calculations were performed for the airfoil at a freestream Mach number of $M_\infty = 0.8$ and zero degrees angle of attack. Comparisons are made with parallel computations performed using the CFL3D[19] code, run in a 2-D mode. The CFL3D code is an Euler/Navier-Stokes code based on cell-centered upwind-difference discretizations of the governing flow equations based on structured meshes. The CFL3D Euler results that were used in the present study were obtained from Ref. 20. Generalized aerodynamic forces for the NACA 0012 airfoil are presented in Fig. 2, computed using the so-called pulse analysis within the unstructured grid Euler code, the unstructured grid Euler harmonic analysis, and the CFL3D harmonic analysis. The results are plotted as real and imaginary components of the unsteady forces, $A_{i,j}$, as a function of reduced frequency k. Plunge and pitch-about-the-quarter-chord motions are defined as modes 1 and 2, respectively. Thus, for example, A_{12} is the lift coefficient due to pitching. Both sets of harmonic results were obtained at six values of reduced frequency: k = 0.0, 0.125, 0.25, 0.5, 0.75, and 1.0. As shown in Fig. 2, the forces from the unstructured grid Euler pulse analysis agree well with the forces from the harmonic analysis. The harmonic analysis, however, is considered to be the more accurate of the two sets of calculations, since the local linearity assumption in the pulse

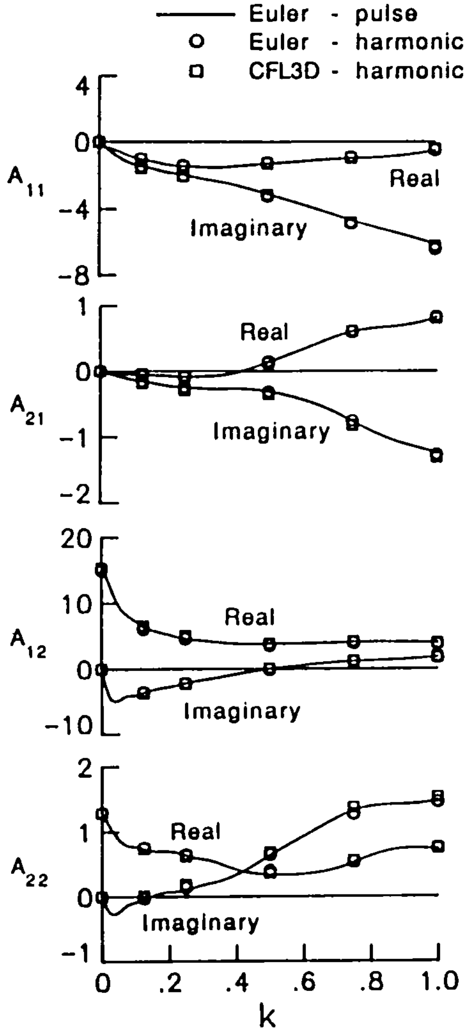

Fig. 2 Comparisons of generalized aerodynamic forces for the NACA 0012 airfoil at $M_\infty = 0.8$ and $\alpha_0 = 0°$ computed using CFL3D and the unstructured-grid central-difference-type Euler flow solver.

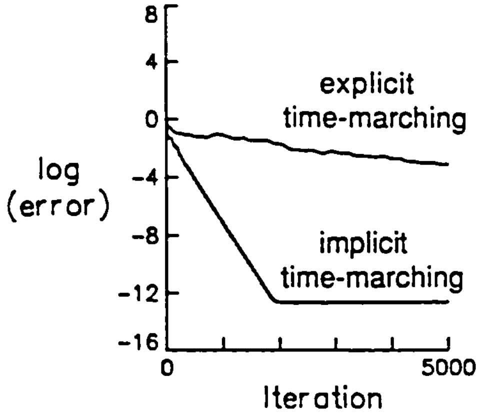

(a) convergence histories.

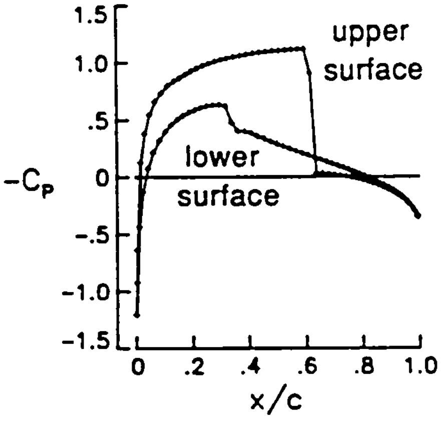

(b) steady pressure distribution.

Fig. 3. Comparisons of steady-state results for the NACA 0012 airfoil at $M_\infty = 0.8$ and $\alpha_0 = 1.25°$ computed using the upwind-type Euler flow solver with flux-vector splitting.

analysis may be questionable for transonic flow cases. As further shown in Fig. 2, the harmonic forces from the unstructured grid Euler code are in very good agreement with the CFL3D (Euler) harmonic forces, for both plunge and pitch motions, for all values of reduced frequency that were considered.

To test the more-recently-developed upwind-type Euler flow solver, steady flow results were obtained for the NACA 0012 airfoil at $M_\infty = 0.8$ and $\alpha_0 = 1.25°$, using both implicit and explicit time-marching. The explicit time-marching results were obtained using a CFL number of 2.5 (since the CFL limit is approximately 2.8) and the implicit time-marching results were obtained using a CFL number of 100,000. Such a large value was used for the implicit results since the relaxation scheme has maximum damping and hence fastest convergence for very large time steps. This is in contrast with implicit approximate factorization schemes which have maximum damping for CFL numbers on the order of 10. A comparison of the convergence histories between explicit and implicit time-marching is shown in Fig. 3(a). The "error" in the solution was taken to be the L_2-norm of the density residual. As shown in Fig. 3(a), the explicit solution is very slow to converge. This solution takes approximately 10,000 time steps to become converged to engineering accuracy, which is taken to be a four order of magnitude reduction in solution error. In contrast, the implicit solution is converged to four orders of magnitude in only approximately 500 steps and is converged to machine zero is less than 2000 steps. The implicit solution costs approximately 75% more per time step than the explicit solution because of the increased number of operations required to evaluate the flux jacobians. This increase in CPU time is far out-weighed by the faster convergence to steady state in that a converged solution is obtained with the implicit relaxation scheme with an order or magnitude less CPU time than the explicit scheme. The resulting steady pressure distribution is shown in Fig. 3(b). For this case there is a relatively strong shock wave on the upper surface of the airfoil near 62% chord and a relatively weak shock wave on the lower surface near 30% chord. The pressure distributions indicate that there is only one grid point within the shock structure, on either the upper or lower surface of the airfoil, due to the sharp shock capturing ability of the upwind-type flow solver.

Unsteady calculations with the upwind-type Euler solver were performed for the airfoil pitching harmonically about the quarter chord with an amplitude of $\alpha_1 = 2.51°$ and a reduced frequency based on semichord of $k = 0.0814$ at $M_\infty = 0.755$ and $\alpha_0 = 0.016°$. These calculations are compared with the experimental data of Ref. 21. Instantaneous pressure distributions at eight points in time during the third cycle of motion using 2500 steps per cycle are shown in Fig. 4 for comparison with the experimental data. In each pressure plot the instantaneous pitch angle $\alpha(\tau)$ and the angular position in the cycle $k\tau$ are noted. During the first part of the cycle there is a shock wave on the upper surface of the airfoil, and the flow over the lower surface is predominately subcritical. During the latter part of the cycle, the flow about the upper surface is subcritical, and a shock forms along the lower surface. The pressure distributions indicate that the shock position oscillates over approximately 25% of the chord along each surface, and in general, that the two sets of calculated

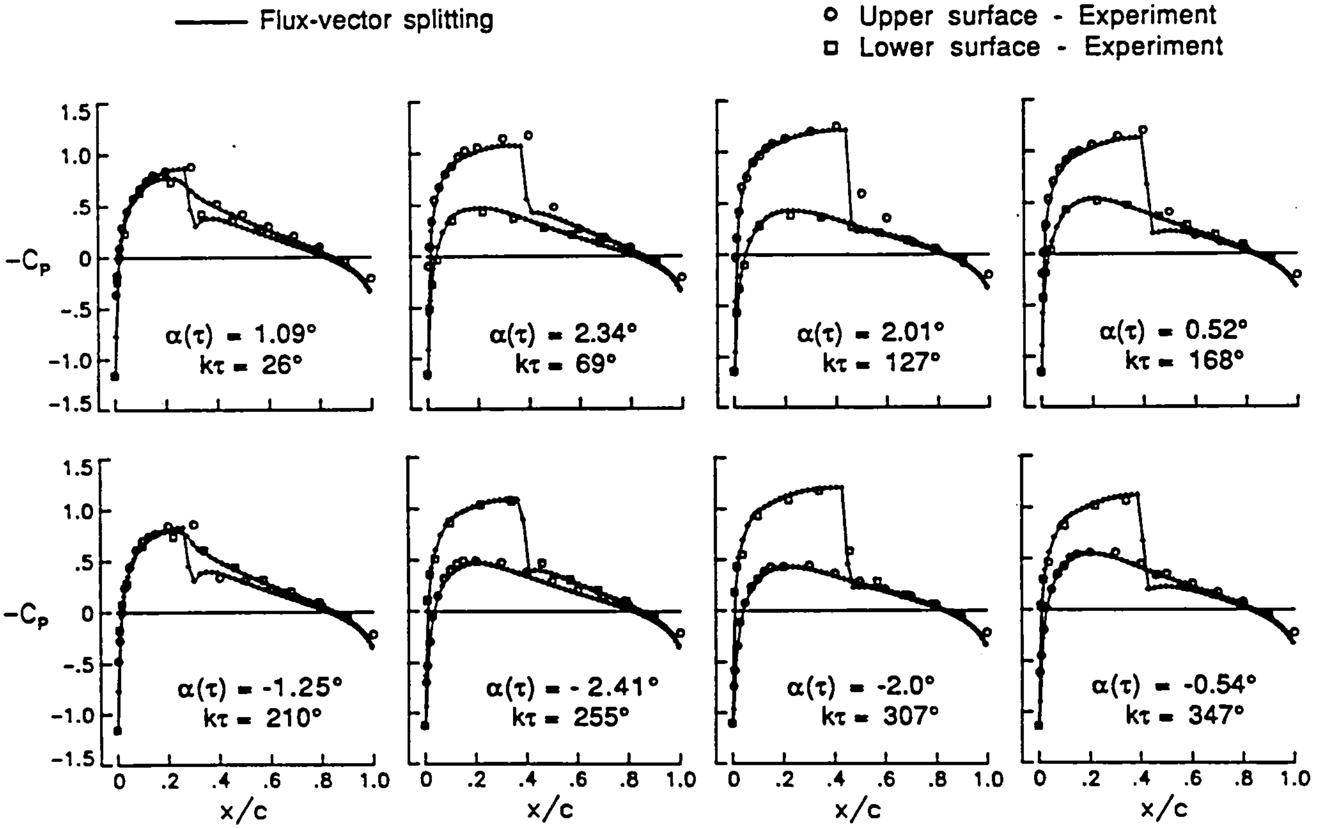

Fig. 4. Comparison of instantaneous pressure distributions for the NACA 0012 airfoil pitching at $M_\infty = 0.755$, $\alpha_0 = 0.016°$, $\alpha_1 = 2.51°$, and $k = 0.0814$ computed using the upwind-type Euler flow solver with flux-vector splitting.

results compare well with the experimental data. Similar to the steady flow results, the shock waves are captured sharply with at most one grid point within the shock structure. The calculated results show the expected symmetry in the flow, in that the upper surface pressure distribution during the first half of the cycle is very similar to the lower surface pressure distribution during the second half of the cycle. A lack of similar symmetry in the experimental results suggests that the data may have been obtained at a slightly higher effective steady-state angle of attack than that reported in Ref. 21. Furthermore, the unstructured grid results of Fig. 4 are of comparable accuracy in comparison with published results obtained using structured grid methods for this case, such as those reported in Ref. 22.

Concial Euler/Navier-Stokes Results

To demonstrate the central-difference-type conical Euler/Navier-Stokes flow solver and the adaptive mesh refinement procedures, calculations were performed for highly-swept delta wing and circular cone cases at high angle of attack and at supersonic freestream flow conditions.[13] In these calculations three cases were considered. In the first two cases, the conical Euler equations were solved for a 75° swept flat-plate delta wing at a freestream Mach number of 1.4. In the first case, steady results were obtained at $\alpha = 20°$ angle of attack and $\beta = 10°$ yaw angle. In the second case, unsteady results were obtained for the wing undergoing a forced harmonic rolling at $\alpha = 20°$ and $\beta = 0°$. For the third

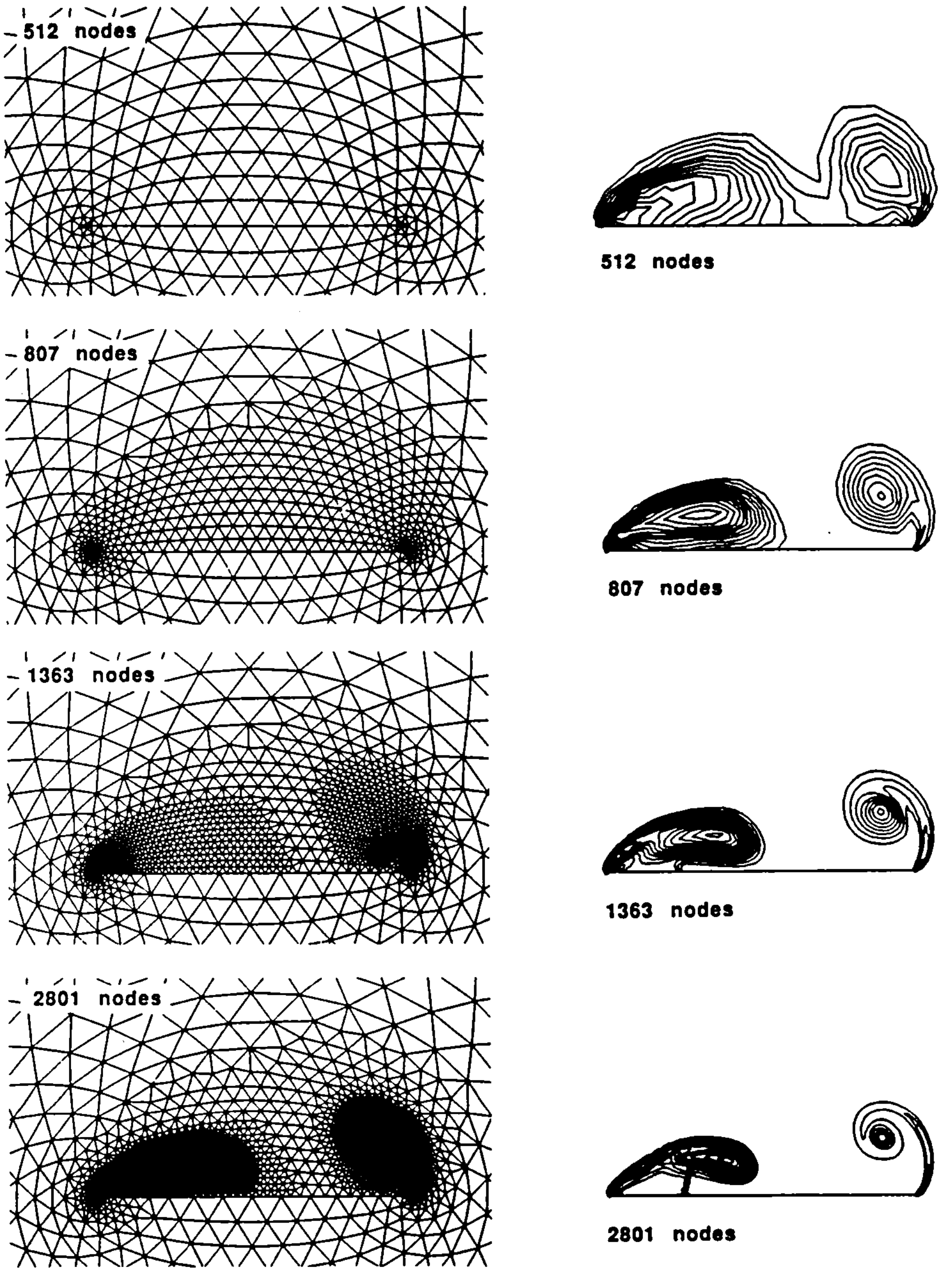

Fig. 5. Effects of adaptive mesh refinement on the total pressure loss contours for a 75° swept flat-plate delta wing at $M_\infty = 1.4$, $\alpha = 20°$, and $\beta = 10°$; computed using the central-difference-type conical Euler flow solver.

case, the conical Navier-Stokes equations were solved for an 85° swept circular cone at $M_\infty = 1.4$, $\alpha = 20°$, $\beta = 0°$, and $Re = 0.5 \times 10^6$.

Case 1. - The first case was selected to demonstrate applications of the adaptive mesh refinement procedures to a wing that is yawed. The calculations were performed by starting with a coarse mesh that has 32 nodes around the wing and 16 nodes in the outward direction for a total of 512 nodes. A partial view of this mesh is shown in the upper left part of Fig. 5. Results were obtained using adaptive mesh refinement by starting with the coarse mesh containing 512 nodes and adapting to the total pressure losses of the instantaneous solution to determine a locally fine mesh. The flow solver was run for a total of 4,000 iterations and the mesh was adapted at iterations 500, 1000, and 1500. Adapting the mesh every 500 iterations produces intermediate results that are converged to plotting accuracy, although this is not a requirement for the adaption procedure to be numerically stable or to produce accurate final results. A summary of the meshes and the corresponding total pressure loss contours is shown in Fig. 5. For this case there is a strong flat vortex produced by the separated flow from the windward (left) leading edge with a crossflow shock wave beneath the vortex. There is also a weaker more-circular vortex produced by the separated flow from the leeward (right) leading edge. With the coarse grids containing 512 (original mesh) and 807 (one enrichment) nodes, the shock wave beneath the windward

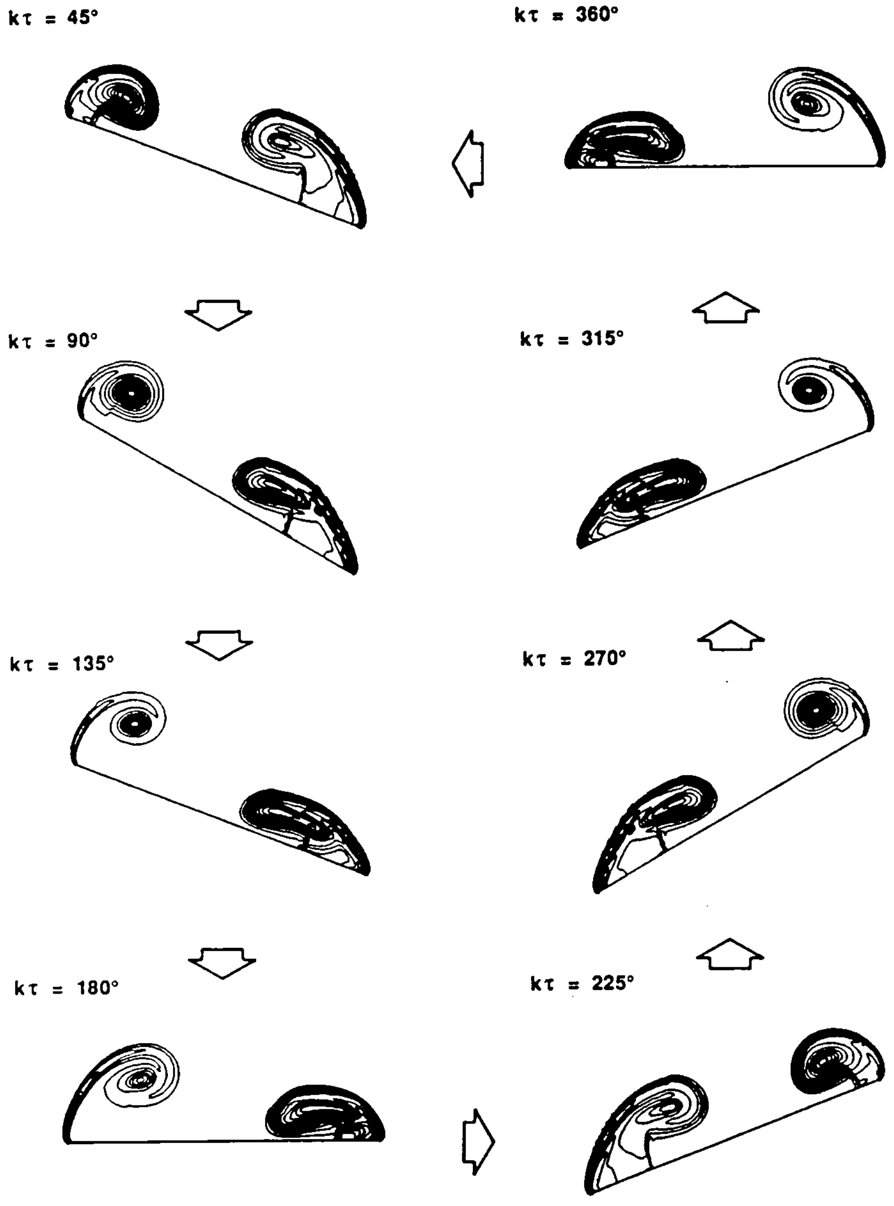

Fig. 6. Instantaneous total pressure loss contours during a cycle of harmonic rolling for a 75° swept flat-plate delta wing at $M_\infty = 1.4$, $\alpha = 20°$, $\beta = 0°$, $\Phi = 30°$, and $k = 0.3$; computed using the central-difference-type conical Euler flow solver.

vortex is not detected in the total pressure loss contours. Upon further enrichment to a grid containing 1363 nodes, the shock begins to appear, and with the final grid of 2801 nodes the shock is shown to be sharply captured. The total pressure loss contours of Fig. 5 indicate that the vortical flow features are more clearly defined when the mesh is adaptively refined. A solution of comparable accuracy on a globally fine mesh would require 32768 nodes (256 x 128). A spatially accurate solution is thus obtained for this case with adaptive mesh refinement, using an order of magnitude fewer grid points (2801 nodes).

Case 2. - The second case was selected to demonstrate the time-accurate capability of the conical Euler flow solver although the results are actually only locally conical. The unsteady results were obtained for the rolling delta wing oscillating harmonically with an amplitude of 30° at $k = 0.3$ using 2400 steps per cycle of motion. In these calculations the grid was first adapted to the steady solution to create a fine embedded mesh locally which was then used in the unsteady calculation. The fine embedded region was made large enough so that the moving vortices and shock waves are always contained within this region and the total grid contained 5152 nodes. It is recognized, however, that for unsteady applications a de-refinement procedure can be used in addition

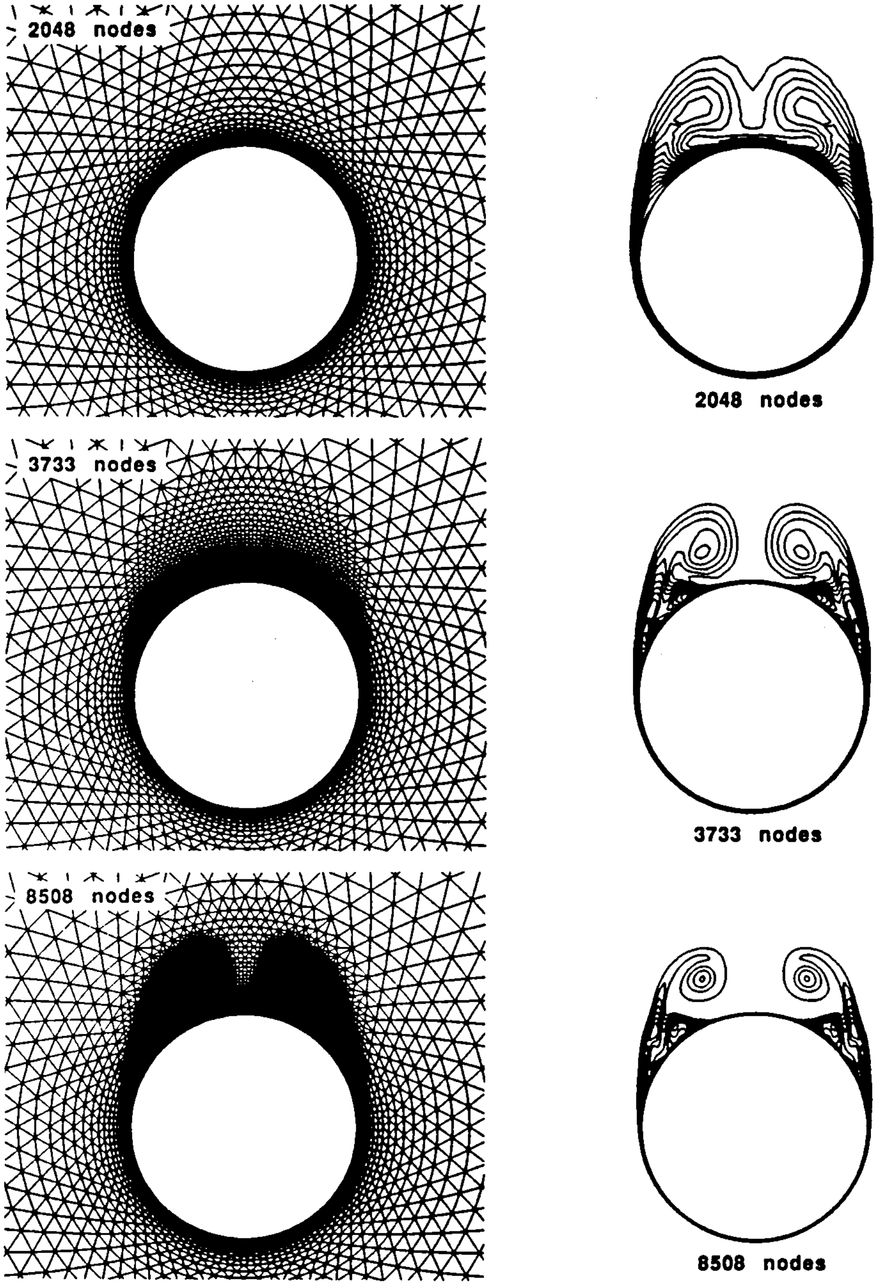

Fig. 7. Effects of adaptive mesh refinement on the total pressure loss contours for an 85° swept circular cone at $M_\infty = 1.4$, $\alpha = 20°$, and $Re = 0.5 \times 10^6$; computed using the central-difference-type conical Navier-Stokes flow solver.

to the refinement procedure, to remove as well as to add nodes and elements during the calculation. Also, during the unsteady calculation the grid was moved as a rigid body to conform to the instantaneous position of the wing. Three cycles of motion were computed to obtain a periodic solution. Instantaneous total pressure loss contours at eight points in time during the third cycle of motion are shown in Fig. 6. In each part of the figure, the instantaneous angular position in the cycle $k\tau$ is noted where τ is time normalized by one-half of the reference length and the streamwise freestream speed.

During the first half of the cycle as the wing rolls clockwise to the maximum amplitude and then back to straight and level, the crossflow shock wave beneath the left vortex disappears, the left vortex weakens, and the right vortex grows in strength. During the second half of the cycle, the opposite situation occurs. The shock wave beneath the right vortex disappears, the right vortex weakens, and the left vortex grows in strength. It is easy to see that the solution is periodic in the third cycle of motion by comparing the total pressure loss contours at any two points in time that are 180° out of phase in the cycle. The two sets of total pressure loss contours, 180° out of phase, are antisymmetric as shown in Fig. 6.

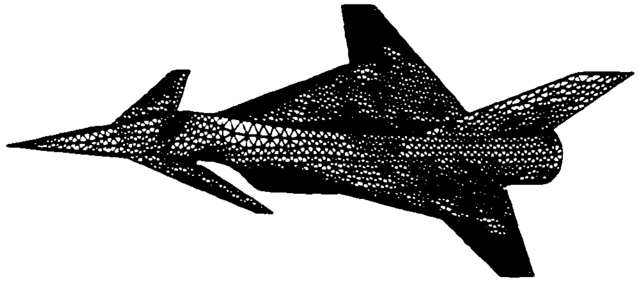

(a) original surface grid.

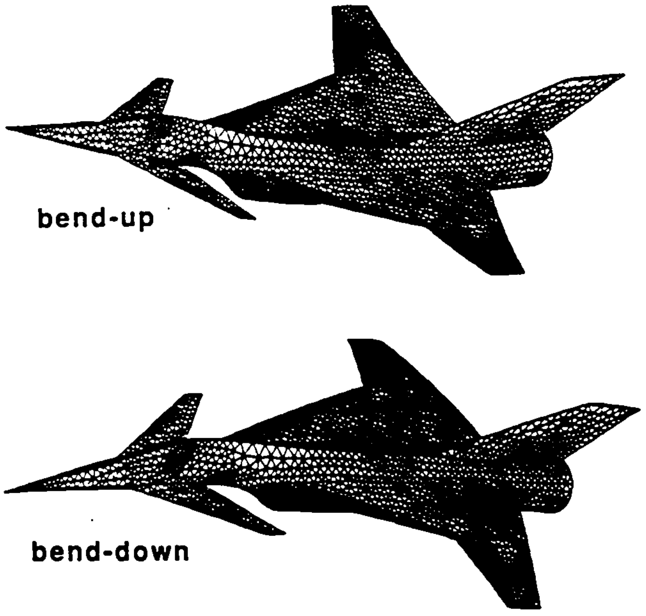

(b) assumed bending mode.

Fig. 8. Surface grid for the Langley supersonic fighter configuration.

Case 3. - The third case was selected to further demonstrate the adaptive mesh refinement procedures for a viscous flow about a circular cone. The calculations were performed by starting with a coarse 64 x 32 mesh (2048 nodes) and adaptively refining the mesh twice. The flow solver was run for a total of 4000 iterations and the mesh was adapted at iterations 1000 and 2000. A summary of the meshes and the corresponding total pressure loss contours is shown in Fig. 7. For this case, there are two large, symmetric, primary vortices that are produced by the separated flow from the left and right sides of the cone. With the coarse mesh containing 2048 nodes, the primary vortices are very diffuse, the secondary vortical flow features are absent, and the boundary layer appears thick. When the grid

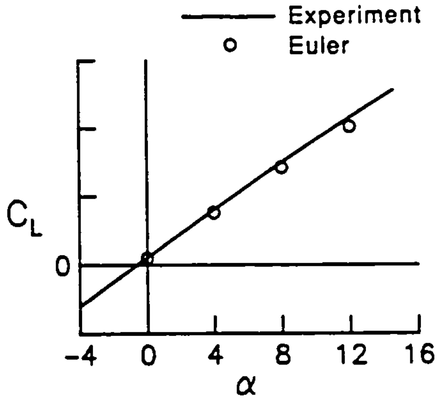

Fig. 9. Comparison of lift coefficient versus angle of attack for the Langley fighter at M_∞ = 2.0 computed using the central-difference-type Euler flow solver.

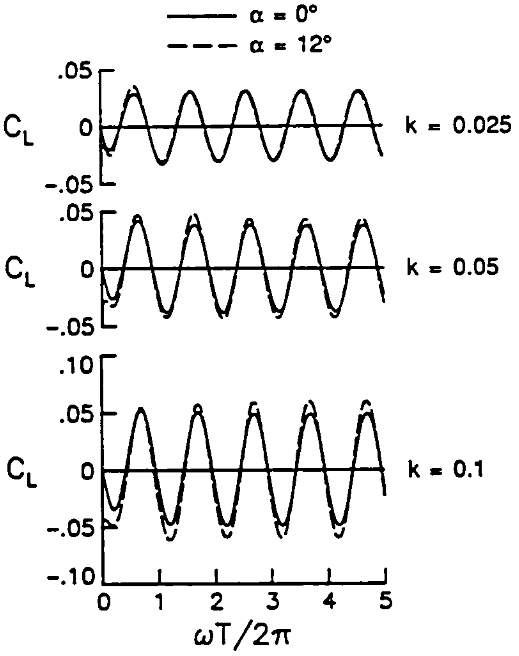

Fig. 10. Effects of angle of attack and reduced frequency on the lift coefficient responses due to the complete vehicle sinusoidal bending deformation of the Langley fighter configuration at M_∞ = 2.0 computed using the central-difference-type Euler flow solver.

is refined to 3733 nodes and then to 8508 nodes, the primary vortices become smaller and more sharply defined, secondary and tertiary vortices become apparent in the flow, and the boundary layer appears to be much thinner in comparison with the coarse grid results. An accurate solution is thus obtained for this case with adaptive mesh refinement, using a factor of approximately four fewer grid points (8508 nodes) in comparison with a globally fine mesh (32768 nodes).

Three-Dimensional Euler Results

To assess the three-dimensional version of the central-difference-type Euler solver and dynamic mesh algorithm, calculations were performed for a supersonic fighter configuration that was tested at NASA Langley Research Center.[12] The fighter will hereafter be referred to as the Langley fighter.[23] The Langley fighter is an aircraft designed to cruise at supersonic Mach numbers and also to manuever efficiently at transonic speeds. The aircraft has a high fineness-ratio fuselage with an underslung swept inlet and a flow-through duct. Other components which make up the configuration include a cranked wing with a leading edge sweep of 70° inboard and 20° outboard, a 55° swept canard, and a 60° swept vertical tail. All of the lifting surfaces have thin circular-arc airfoil sections. Results were obtained for the Langley fighter using a grid which has 13,832 nodes and 70,125 tetrahedra. The surface triangulation of the aircraft is shown in Fig. 8(a). Because of symmetry, the calculations were performed for only half of the aircraft which contained 4581 triangles on the surface of the vehicle. Steady-state results were obtained for the Langley fighter at a freestream Mach number of 2.0 and four angles of attack including α = 0°, 4°, 8°, and 12°. Unsteady results were obtained at α = 0° and 12° for the aircraft oscillating harmonically in an assumed polynomial complete-vehicle bending mode which is shown in Fig. 8(b). Three values of reduced frequency based on wing tip semi-chord were considered including k= 0.025, 0.05, and 0.1. The amplitude of the deformation was taken to be one-fifth of the mode shape shown in the figure. So, for example, the wing tip deflection in the calculation was approximately 20% of the tip chord.

Steady flow results were obtained for the Langley fighter configuration using 1500 iterations starting from freestream flow conditions. Convergence to steady-state was accelerated using local time-stepping, implicit residual smoothing, and enthalpy damping. In each case, the error in the solution, as defined by the L_2-norm of the density residual, was reduced by approximately four orders of magnitude. Detailed color-contour plots of the pressure coefficients on the surface of the vehicle were presented in Ref. 12. A comparison between calculated and experimental lift coefficient versus angle of attack for the Langley fighter is shown in Fig. 9. In general, the calculated lift coefficient agrees well with the experimental data, especially at the lower angles of attack of 0° and 4°. At the higher angles of attack of 8° and 12°, the calculated lift is slightly underpredicted in comparison with the measured values, which is possibly due to the coarseness of the grid.

Unsteady flow results were obtained for the Langley fighter configuration oscillating harmonically in the complete-vehicle bending mode. The calculations were performed for k = 0.025, 0.05, and 0.1 using 1440, 720, and 360 steps per cycle of motion, respectively, for five cycles. Calculated instantaneous pressure contours at the maximum (bend-up) and minimum (bend-down) amplitudes of oscillation, during the fifth cycle, were presented in Ref. 12. Lift coefficient responses for the fighter oscillating at $M_\infty = 2.0$ are presented in Fig. 10. To quantify the effects of angle of attack and reduced frequency, five cycles of motion were considered as plotted. In each case, the mean value of the oscillating lift was subtracted off to allow for a direct comparison between results obtained at α = 0° and α = 12°. As shown in Fig. 10, the effects of angle of attack are very small for k = 0.025. As the reduced frequency is increased, however, the magnitudes of the response of the aircraft increase and there is a small change in phase of approximately 35°. Also, an effect due to angle of attack becomes evident, in that the responses at α = 12° are of larger magnitude than those at α = 0°. This effect is possibly attributable to a small amount of vortical flow that is present along the upper surface of the wings in the inboard region at α = 12°.

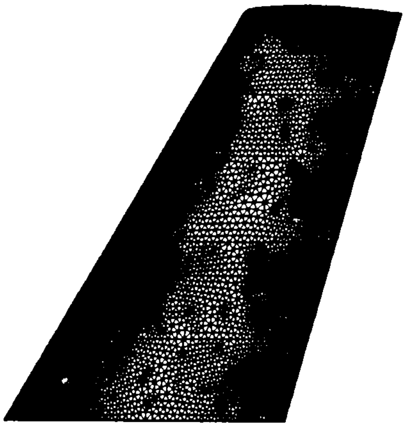

Fig. 11. Upper surface grid for the ONERA M6 wing.

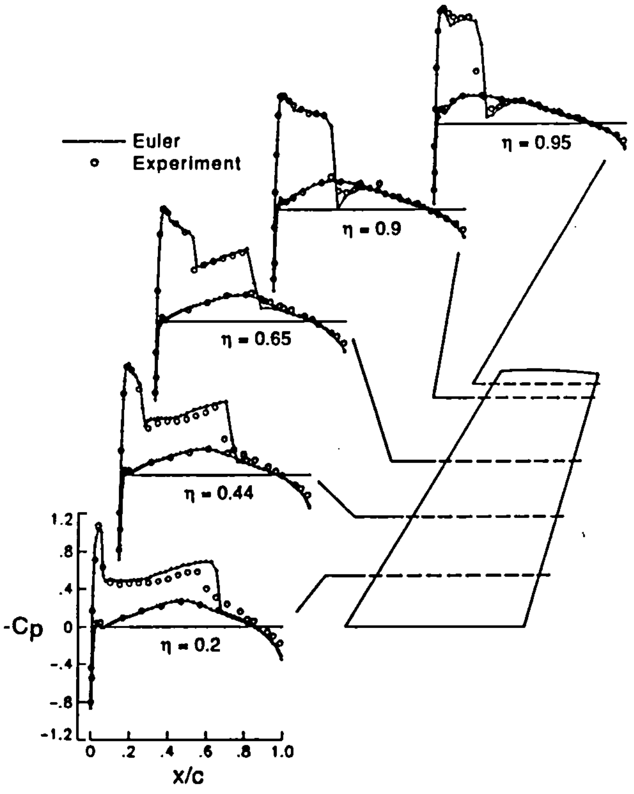

Fig. 12. Comparisons of steady pressure distributions for the ONERA M6 wing at $M_\infty = 0.84$ and $\alpha_0 = 3.06°$ computed using the upwind-type Euler flow solver with flux-vector splitting.

To test the more-recently-developed upwind-type Euler flow solver, calculations were performed for the ONERA M6 wing.[24] The M6 wing has a leading edge sweep angle of 30°, an aspect ratio of 3.8, and a taper ratio of 0.562. The airfoil section of the wing is the ONERA "D" airfoil which is a 10% maximum thickness-to-chord ratio conventional section. The results were obtained using a grid which has 154,314 nodes and 869,056 tetrahedra. The surface triangulation for the upper surface of the wing is shown in Fig. 11. Results were obtained for the M6 wing at a freestream Mach number of 0.84 and 3.06° angle of attack. These conditions were chosen for comparison with the experimental pressure data of Ref. 24. The results were obtained using the explicit time-marching scheme since it requires half of the memory of the implicit scheme. The code was run for 6000 time steps at a CFL number of 5.0, which produced a four order of magnitude reduction in the L_2-norm of the density residual.

Figure 12 shows surface pressure coefficient comparisons with the experimental data at five span stations including η = 0.2, 0.44, 0.65, 0.9, and 0.95. In these plots the Euler results are given by the solid curves where plus signs have been included to indicate the actual grid point values which are connected with straight line segments. The experimental data is represented by the circles. For $\eta = 0.2$ there are two shock waves along the chord. The forward shock wave is well predicted including the suction peak. The second shock wave is predicted slightly downstream of the experimental shock location which is typical of inviscid methods for this case. Also, the lower surface pressure coefficients agree well with the data. At $\eta = 0.44$ the shock locations have begun to coalesce. The leading edge suction peak is well predicted and both shock waves are captured sharply. At $\eta = 0.65$ the forward shock wave is near 20% chord and the second shock wave is near midchord. All of the pressure levels are well predicted and both shocks are captured sharply with only one grid point within the shock structure. There are also no overshoots or undershoots near the shocks due to the flux limiting. Furthermore, the lower surface pressure coefficients are predicted accurately. At $\eta = 0.9$ the two shocks have merged to form a single, relatively strong, shock wave near 25% chord. Here the shock is very sharply captured and the calculated pressures again agree well with the experimental data. Finally at $\eta = 0.95$, the shock wave is slightly stronger than the previous span station. Here, the calculated shock again has only one interior point.

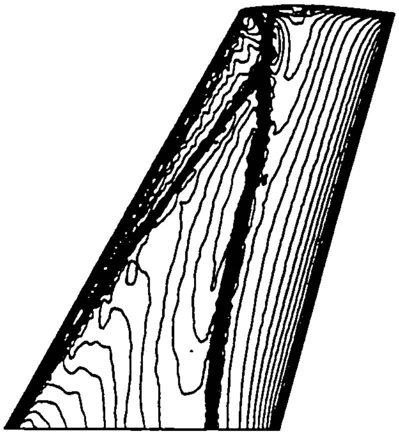

(a) upper surface.

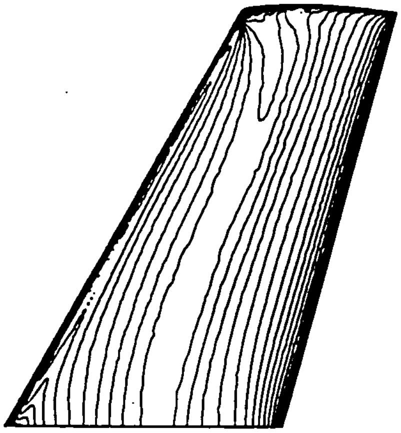

(b) lower surface.

Fig. 13. Surface pressure contour lines ($\Delta p = 0.02$) on the ONERA M6 wing at $M_\infty = 0.84$ and $\alpha_0 = 3.06°$ computed using the upwind-type Euler flow solver with flux-vector splitting.

Figure 13 shows pressure contour lines on the surface of the wing plotted using an increment of $\Delta p = 0.02$. Pressure contours on the upper surface are shown in Fig. 13(a); Pressure contours on the lower surface are shown in Fig. 13(b). The upper surface contours (Fig. 13(a)) clearly show the lambda-type shock wave pattern formed by the two inboard shock waves which merge together near 80% semispan to form the single strong shock wave in the outboard region of the wing. The lower surface contours (Fig. 13(b)) indicate that there is very little spanwise variation in pressure.

Concluding Remarks

The current status of the development of unstructured grid methods in the Unsteady Aerodynamics Branch at NASA Langley Research Center was described. These methods are being developed for steady and unsteady aerodynamic applications. The paper highlighted the flow solvers that have been developed for the solution of the unsteady Euler and Navier-Stokes equations and gave selected results which demonstrated various features of the capability. The results demonstrated two- and three-dimensional applications for both steady and unsteady flows. Comparisons were also made with solutions obtained using a structured grid code and with experimental data to determine the accuracy of the unstructured grid methodology. These comparisons showed good agreement which thus verified the accuracy.

References

[1]Jameson, A.: "Successes and Challenges in Computational Aerodynamics," AIAA Paper No. 87-1184, January 1987.

[2]Edwards, J. W.; and Thomas, J. L.: "Computational Methods for Unsteady Transonic Flows," AIAA Paper No. 87-0107, January 1987. Also chapter 5 in Unsteady Transonic Aerodynamics, ed. by D. Nixon, vol. 120 in AIAA Progress in Astronautics and Aeronautics, September 1989.

[3]Jameson, A.; and Mavriplis, D. J.: "Finite Volume Solution of the Two-Dimensional Euler Equations on a Regular Triangular Mesh," AIAA Journal, vol. 24, April 1986, pp. 611-618.

[4] Mavriplis, D. J.: "Multigrid Solution of the Two-Dimensional Euler Equations on Unstructured Triangular Meshes," AIAA Journal, vol. 26, July 1988, pp. 824-831.

[5] Jameson, A.; Baker, T. J.; and Weatherill, N. P.: "Calculation of Inviscid Transonic Flow Over a Complete Aircraft," AIAA Paper No. 86-0103, January 1986.

[6] Morgan, K.; and Peraire, J.: "Finite Element Methods for Compressible Flow," Von Karman Institute for Fluid Dynamics Lecture Series 1987-04, Computational Fluid Dynamics, March 2-6, 1987.

[7] Lohner, R.: "Finite Elements in CFD: What Lies Ahead," International Journal for Numerical Methods in Engineering, vol. 24, 1987, pp. 1741-1756.

[8] Morgan, K.; Peraire, J.; Thareja, R. R.; and Stewart, J. R.: "An Adaptive Finite Element Scheme for the Euler and Navier-Stokes Equations," AIAA Paper No. 87-1172, 1987.

[9] Peraire, J.; Peiro, J.; Formaggia, L.; and Morgan, K.: "Finite Element Euler Computations in Three Dimensions," AIAA Paper No. 88-0032, January 1988.

[10] Batina, J. T.: "Unsteady Euler Airfoil Solutions Using Unstructured Dynamic Meshes," AIAA Paper No. 89-0115, January 1989.

[11] Rausch, R. D.; Batina, J. T.; and Yang, H. T.: "Euler Flutter Analysis of Airfoils Using Unstructured Dynamic Meshes," AIAA Paper No. 89-1384, April 1989.

[12] Batina, J. T.: "Unsteady Euler Algorithm with Unstructured Dynamic Mesh for Complex-Aircraft Aeroelastic Analysis," AIAA Paper No. 89-1189, April 1989.

[13] Batina, J. T.: "Vortex-Dominated Conical-Flow Computations Using Unstructured Adaptively-Refined Meshes," AIAA Paper No. 89-1816, June 1989.

[14] Batina, J. T.: "Implicit Flux-Split Euler Schemes for Unsteady Aerodynamic Analysis Involving Unstructured Dynamic Meshes," AIAA Paper No. 90-0936, April 1990.

[15] Batina, J. T.: "Accuracy of an Unstructured-Grid Upwind-Euler Algorithm for the ONERA M6 Wing," presented at the Accuracy of Unstructured Grid Techniques Workshop, NASA Langley Research Center, Hampton, Virginia, January 16-17, 1990.

[16] Batina, J. T.: "Three-Dimensional Flux-Split Euler Schemes Involving Unstructured Dynamic Meshes," AIAA Paper No. 90-1649, June 1990.

[17] Van Leer, B.: "Flux-Vector Splitting for the Euler Equations," Lecture Notes in Physics, vol. 170, 1982, pp. 507-512.

[18] Roe, P. L.: "Approximate Riemann Solvers, Parameter Vectors, and Difference Schemes," Journal of Computational Physics, vol. 43, 1981, pp. 357-372.

[19] Anderson, W. K.; Thomas, J. L.; and Rumsey, C. L.: "Extension and Application of Flux-Vector Splitting to Unsteady Calculations on Dynamic Meshes," AIAA Paper No. 87-1152, June 1987.

[20] Robinson, B. A.; Batina, J. T.; and Yang, T. Y.: "Aeroelastic Analysis of Wings Using the Euler Equations With a Deforming Mesh," AIAA Paper No. 90-1032, April 1990.

[21] Landon, R. H.: "NACA 0012. Oscillating and Transient Pitching," Data Set 3 in AGARD-R-702, Compendium of Unsteady Aerodynamic Measurements, August 1982.

[22] Anderson, W. K.; and Batina, J. T.: "Accurate Solutions, Parameter Studies, and Comparisons for the Euler and Potential Flow Equations," paper No. 14, AGARD CP-437, May 1988.

[23] Hom, K. W.; and Ticatch, L. A.: "Investigation of an Advanced Supersonic Fighter Concept Including Effects of Horizontal Tail and Canard Control Surfaces Over a Mach Number Range From 1.6 to 2.5," NASA TP-2526, May 1986.

[24] Schmitt, V.; and Charpin, F.: "Pressure Distribution on the ONERA M6 Wing at Transonic Mach Numbers," Appendix B1 in AGARD-AR-138, Experimental Data Base for Computer Program Assessment, May 1979.

NASA
National Aeronautics and Space Administration

Report Documentation Page

1. Report No. NASA TM-102730	2. Government Accession No.	3. Recipient's Catalog No.

4. Title and Subtitle Development of Unstructured Grid Methods for Steady and Unsteady Aerodynamic Analysis	5. Report Date November 1990
	6. Performing Organization Code
7. Author(s) John T. Batina	8. Performing Organization Report No.
	10. Work Unit No. 505-63-50-12
9. Performing Organization Name and Address NASA Langley Research Center Hampton, Virginia 23665-5225	11. Contract or Grant No.
	13. Type of Report and Period Covered Technical Memorandum
12. Sponsoring Agency Name and Address National Aeronautics and Space Administration Washington, DC 20546-0001	14. Sponsoring Agency Code

15. Supplementary Notes

Presented as Paper ICAS-90-6.9.4 at the 17th Congress of the International Council of the Aeronautical Sciences, Stockholm, Sweden, September 10-13, 1990.

16. Abstract

The current status of the development of unstructured grid methods in the Unsteady Aerodynamics Branch at NASA Langley Research Center is described. These methods are being developed for steady and unsteady aerodynamic applications. The paper first highlights the flow solvers that have been developed for the solution of the unsteady Euler and Navier-Stokes equations and then gives selected results which demonstrate various features of the capability. The results demonstrate two- and three-dimensional applications for both steady and unsteady flows. Comparisons are also made with solutions obtained using a structured grid code and with experimental data to determine the accuracy of the unstructured grid methodology. These comparisons show godd agreement which thus verifies the accuracy.

17. Key Words (Suggested by Author(s)) Unsteady Aerodynamics Computational Fluid Dynamics Transonic Flow Vortical Flow	18. Distribution Statement Unclassified - Unlimited Subject Category 02

19. Security Classif. (of this report) Unclassified	20. Security Classif. (of this page) Unclassified	21. No. of pages 12	22. Price A03

NASA FORM 1626 OCT 86